ACS APPLIED NANO MATERIALS

www.acsanm.org Article

# Dielectric Effects in $FeO_x$-Coated Au Nanoparticles Boost the Magnetoplasmonic Response: Implications for Active Plasmonic Devices

Alessio Gabbani,[▽] Elvira Fantechi,[▽] Gaia Petrucci, Giulio Campo, César de Julián Fernández, Paolo Ghigna, Lorenzo Sorace, Valentina Bonanni, Massimo Gurioli, Claudio Sangregorio, and Francesco Pineider*

Cite This: *ACS Appl. Nano Mater.* 2021, 4, 1057−1066 Read Online

ACCESS | Metrics & More | Article Recommendations | Supporting Information

**ABSTRACT:** Plasmon resonance modulation with an external magnetic field (magnetoplasmonics) represents a promising route for the improvement of the sensitivity of plasmon-based refractometric sensing. To this purpose, an accurate material choice is needed to realize hybrid nanostructures with an improved magnetoplasmonic response. In this work, we prepared core@shell nanostructures made of an 8 nm Au core surrounded by an ultrathin iron oxide shell (≤1 nm). The presence of the iron oxide shell was found to significantly enhance the magneto-optical response of the noble metal in the localized surface plasmon region, compared with uncoated Au nanoparticles. With the support of an analytical model, we ascribed the origin of the enhancement to the shell-induced increase in the dielectric permittivity around the Au core. The experiment points out the importance of the spectral position of the plasmonic resonance in determining the magnitude of the magnetoplasmonic response. Moreover, the analytical model proposed here represents a powerful predictive tool for the quantification of the magnetoplasmonic effect based on resonance position engineering, which has significant implications for the design of active magnetoplasmonic devices.

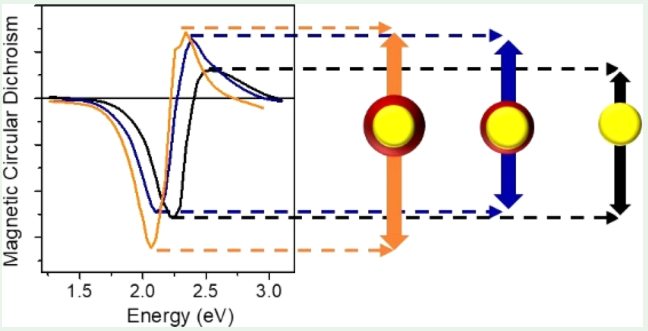


**KEYWORDS:** *magnetoplasmonics, gold@iron oxide core−shell, nanoheterostructures, magnetic circular dichroism, plasmonics, active plasmonics*

## INTRODUCTION

In recent years, plasmonics has received rapidly growing interest for scientific and technological applications. Indeed, thanks to the extralocalization of the electric field of light in the nanosize region combined with the strong dependence of localized surface plasmon resonance (LSPR) on the refractive index of the medium, plasmonic nanomaterials are excellent candidates for applications in nanophotonics and optical sensing.[1−4] Nowadays, one of the major challenges in the field is the possibility of actively controlling the plasmonic response with an external agent, with the aim of precisely and reversibly modulating the electronic and optical properties of the plasmonic material, thus expanding the exploitable technological areas.[5−10] Within this framework, one of the more promising routes is magnetoplasmonics, which uses an external magnetic field for this aim and may open the way for significant innovations in refractometric sensing (increasing the sensitivity by fast modulation of the plasmonic response),[11,12] light guiding, non-reciprocal optics, and optomagnetism.[13−17]

It has been recently demonstrated that magnetic modulation of LSPR can be achieved on purely plasmonic resonators, such as colloidal dispersions of spherical gold nanoparticles (NPs) or nanodisks. Such modulation of the optical features results in a static, phase-locked signal in magneto-optical (MO) spectroscopic techniques.[11,18] Preliminary reports on the benefit of magnetic modulation to improve the sensitivity of plasmonic refractometric sensing were presented for plasmonic Au nanospheres and magnetoplasmonic Ni nanodisks.[11,12,19] While for noble metal nanostructures, the magnetic modulation of LSPR is rather small, significant improvements can be achieved by the accurate design of the nanostructures. Among the approaches reported, the exploitation of robust and reproducible electron beam lithography allowed the fabrication of nanomaterials with improved magnetoplasmonic features, for instance, using a magnetic metal able to sustain a plasmonic

**Received:** September 24, 2020
**Accepted:** December 31, 2020
**Published:** January 21, 2021

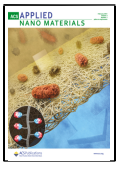







https://dx.doi.org/10.1021/acsanm.0c02588
*ACS Appl. Nano Mater.* 2021, 4, 1057−1066

resonance (such as Ni nanowires[20] or nanodisks[12,21,22]) or by designing appropriate hybrid magnetoplasmonic nanoheterostructures, in which noble metals are directly combined with magnetic metals[23,24] or metal alloys[25−28] at the nanoscale. Improved magnetoplasmonic performance was also achieved by embedding Au nanostructures in a magneto-optically active Bi:YIG film.[29] An alternative to physical methods, chemical synthesis is a valuable and complementary tool as it can produce higher amounts of hybrid nanoheterostructures with good control over size, shape, and composition, which are readily dispersible in transparent solvents or polymeric matrices.[30−35] However, only a few examples of hybrid nanostructures with promising magnetoplasmonic properties have been reported through these approaches.[36−39] Moreover, the investigation was almost exclusively focused on the effect of LSPR on the MO activity of the magnetic counterpart, rather than on the possible role of the latter in the magnetic modulation of the LSPR in the noble metal domain. This is probably due to two main factors: (i) the addition of a magnetic material to the plasmonic resonator usually causes the damping of the LSPR, decreasing its figure of merit and (ii) the MO signal of the magnetic material is often predominant with respect to the plasmonic one, thus masking the interesting effects taking place around the plasmonic resonance. It follows that reaching a fine balance between the magnetic and the plasmonic counterparts is of paramount importance in order to design efficient magnetoplasmonic nanoheterostructures, and new strategies to enhance the magnetic modulation of LSPR without adding lossy magnetic materials would be desirable. This is particularly important in gold−iron oxide heterostructures, where usually the magneto-optical signal of the iron oxide phase is dominant and it is at least 1−2 orders of magnitude larger than that of noble metal NPs.[40,41]

Here, we report the investigation of a magneto-plasmonic gold@iron oxide core@shell nanostructure with an ultrathin shell (≤1 nm), prepared by a wet chemistry approach. The core@shell morphology allows achieving a high degree of interaction between the magnetic and the plasmonic counterparts, and the LSPR is expected to depend both on the thickness of the shell as well as on its dielectric function, introducing additional degrees of freedom in the control of the LSPR. The formation of the iron oxide phase was confirmed by a detailed analysis carried out using different structural and magnetic techniques, and its presence induced a significant increase of the magnetic circular dichroism (MCD) signal of the plasmonic core with respect to that of uncovered gold nanoparticles, despite displaying a negligible magnetic response. The origin of such an increase in the magnetic modulation of LSPR was analyzed in terms of an analytical model developed in a previous work for spherical plasmonic NPs.[11] Our investigation reveals that a crucial role is played by the dielectric permittivity of the shell, suggesting a novel strategy to improve the MO signal, which is critical for magnetoplasmonic refractometric sensing. In particular, by controlling the LSPR spectral position, it is possible to modify the amplitude of its magneto-optical response, allowing an enhancement of up to 50%. This is particularly relevant in indirect nanoplasmonic sensing experiments, in which a dielectric layer surrounds the plasmonic unit.[3] Such a dielectric layer can be for instance a silica coating protecting the material from oxidation or the support for a nanostructured catalyst.[3,42,43] The LSPR response of the plasmonic nanostructure can also be used to probe changes in dielectric films deposited on top of it, i.e., to probe shrinking−swelling transitions in a hydrogel film[44] or phase transitions occurring within an inorganic film.[45,46] Our results demonstrate that the magnetoplasmonic response benefits from the presence of a dielectric layer around Au NPs, providing a promising strategy for the design of nanomaterials with improved magnetoplasmonic performance, which has interesting implications in nanoplasmonic sensing and other active plasmonic nanodevices.

## EXPERIMENTAL SECTION

**Materials.** All samples were prepared under a nitrogen atmosphere using commercially available reagents. Tetralin (99%), oleylamine (OAm) (70%), oleic acid (OA) (90%), iron(III) acetylacetonate ($Fe(acac)_3$) (≥99.9%), benzyl ether (≥98%), hexane (≥95%), and ethanol (96%) were purchased from Aldrich Chemical Co. Gold(III) chloride trihydrate ($HAuCl_4{\cdot}3H_2O$) (≥ 99.9%) was purchased from Strem Chemicals Co.

**Synthesis of 8 nm Au NPs.** Colloidal Au NPs were prepared by reduction of $Au^{3+}$ chloride trihydrate ($HAuCl_4{\cdot}3H_2O$) by oleylamine in tetralin, following the procedure reported by Yu *et al.*[47] Briefly, $HAuCl_4{\cdot}3H_2O$ (1.0 g, 2.5 mmol) was mixed with oleylamine (10 mL, 30 mmol) in tetralin (100 mL), and the mixture was heated to 65 °C and kept at this temperature for 5 h. The mixture was cooled to room temperature by removing the heat source, and Au NPs were separated by the addition of EtOH and successive centrifugation (4000 rpm, 10 min). This washing procedure was repeated twice. The obtained NPs are surrounded by a layer of oleylamine, which ensures colloidal stabilization and makes them readily dispersed in hexane or other apolar solvents.

**Synthesis of CS1 NPs.** A mixture of Au NPs (0.011 g in ∼5 mL of hexane), $Fe(acac)_3$ (0.088 g, 0.25 mmol), oleylamine (0.53 g, 2 mmol), and oleic acid (0.57 g, 2 mmol) in 50 mL of benzyl ether was heated up to 205 °C under nitrogen flow and kept at this temperature for 2 h. The reaction mixture was cooled to room temperature under a nitrogen atmosphere by removing the heating source. The obtained $Au@FeO_x$ core@shell NPs were separated by centrifuging the reaction mixture twice with EtOH and further redispersion in hexane. The resulting nanoparticles are surrounded by a layer of capping agents (oleic acid and oleylamine), making them dispersible in apolar solvents.

**Synthesis of CS2 NPs.** CS2 NPs were obtained using the same synthetic procedure but using CS1 as the starting seeds instead of Au NPs.

**Structural and Magnetic Characterization.** Morphology and particle size distribution were determined by transmission electron microscopy (TEM), using a CM12 PHILIPS microscope operating at 100 kV. Samples were prepared by drop drying a dilute suspension of nanoparticles in hexane onto 200 mesh carbon-coated copper grids. The mean size and size distribution were obtained from statistical analysis over 200 nanoparticles.

Fluorescence XAS (X-ray absorption spectroscopy) data were collected at the ID12 beamline (European Synchrotron Radiation Facility, ESRF, Grenoble, experiment HE-3431) at the Fe-K edge,[48] at $T$ = 7 K. Samples were drop-casted from a $CH_3Cl$ suspension on the sample holder. For the XANES (X-ray absorption near-edge structure) analysis, the spectra were processed by subtracting the smooth pre-edge background fitted with a straight line. The spectra were normalized at unit absorption.

Magnetic measurements were performed using a Quantum Design MPMS SQUID, operating in the 1.8−350 K temperature range and with an applied field up to 5 T. The samples were deposited from hexane suspensions onto a Teflon sample holder, and the diamagnetic contribution was corrected during data processing.

X-band (9.39 GHz) EPR spectra were acquired using a Bruker Elexsys E500 spectrometer equipped with an SHQE cylindrical cavity and a continuous-flow $^4$He cryostat (ESR 900, Oxford Instruments) for measurements at variable temperatures.


https://dx.doi.org/10.1021/acsanm.0c02588
ACS Appl. Nano Mater. 2021, 4, 1057−1066

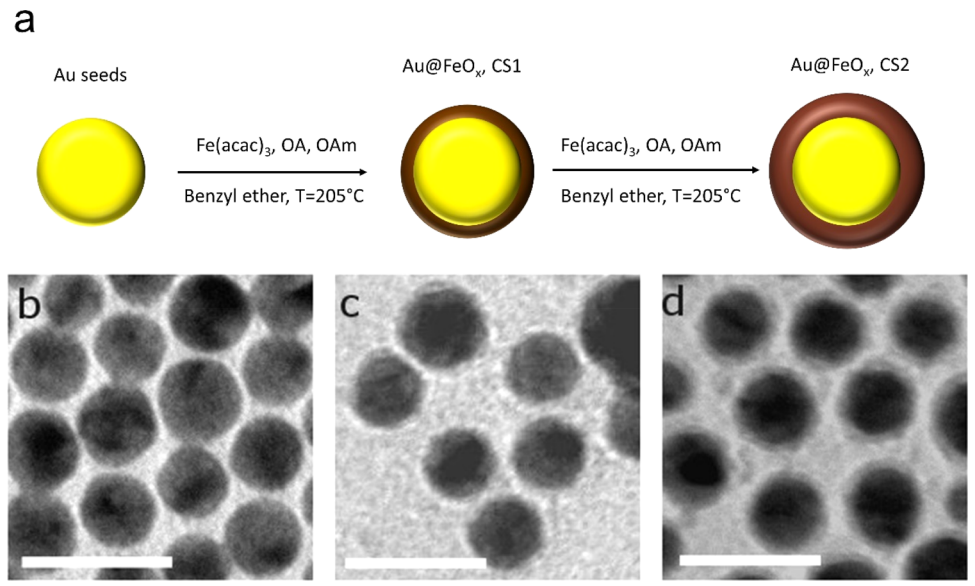


**Figure 1.** (a) Schematic representation of nanostructured magnetoplasmonic Au@FeO$_x$ core@shell NPs with different iron oxide shell thicknesses; (b–d) representative TEM images of Au NPs (b), CS1 (c), and CS2 (d). Scale bar is 20 nm.

**Optical and Magneto-optical Characterization.** Extinction spectra have been recorded on a JASCO V-670 commercial spectrophotometer in the 300–1000 nm range using 1 mm quartz cuvettes. The obtained spectra, reported as absorbance *vs* energy (eV), were fitted with a combination of a Lorentzian and a Gaussian function for the plasmon resonance peak and the interband transition, respectively. MCD signals were recorded using a home-built setup[49] equipped with a 250 W Hg-Xe arc lamp, an Oriel 1/8 m Cornerstone 130 monochromator, and a liquid-cooled electromagnet. The setup covers a wavelength range from 400 to 1000 nm and reaches static fields up to 1.35 T at room temperature. Light propagation was set parallel to the static magnetic field. Circular polarization was obtained using a photo-elastic modulator (Hinds Instruments PEM-90) able to switch at a rate of 50 kHz between right- and left-circular light polarization, and dichroism was recorded by lock-in detection at the modulation frequency. To avoid offset issues and natural dichroism coming from the setup, the final MCD spectrum is obtained by subtraction of two spectra recorded at the same magnetic field but with opposite signs. The magnitude of the dichroism signal ($\Delta A$) was calibrated through a standard technique using an $Fe(CN)_6^{3+}$ solution as a reference. Measurements were performed on hexane solutions of samples, and in order to take into account the different concentrations of the colloidal dispersions investigated, the MCD spectra were normalized with respect to the extinction maximum of the LSPR peak and to the value of applied magnetic field (1.35 T). Fixed wavelength field-dependent MCD was acquired at room temperature on sample CS2 dispersed in a transparent polystyrene matrix.

## RESULTS AND DISCUSSION

**Synthesis and Structural Characterization.** Au@FeO$_x$ NPs were prepared by thermal decomposition of iron(III) acetyl acetonate (Fe(acac)$_3$) in benzyl ether, following a seeded-growth approach in which the iron oxide nucleation and growth occur on the surface of preformed gold nanoparticles (Au NPs) used as seeds. The synthetic conditions were adjusted in order to promote the hetero-nucleation and growth of a very thin layer of iron oxide: in this way, by cyclically repeating the synthesis, it was possible to add an additional thin iron oxide layer and to finely control the final thickness of the iron oxide shell. Two nanostructured magnetoplasmonic gold@iron oxide core–shell (Au@FeO$_x$) systems were prepared, with increasing shell thickness of the iron oxide layer (0.5 and 1.0 nm for samples CS1 and CS2, respectively; Figure 1). TEM images, reported in Figure 1b–d, show the presence of a thin layer with a lower contrast surrounding the Au domain, indicating the successful formation of the core@shell structure. The average mean size was found to increase from 8 ± 2 nm for Au NPs to 9 ± 2 nm and 10 ± 2 nm for CS1 and CS2, respectively (size distributions are reported in Figure S1).

The presence of the iron oxide phase was further confirmed by a detailed spectroscopic characterization through X-ray absorption spectroscopy (XAS) and electron paramagnetic resonance (EPR). XAS analysis was performed at the Fe edge for sample CS1. The edge energy position of CS1 is almost coincident with that of $\gamma$-Fe$_2$O$_3$, which indicates a nominal $Fe^{3+}$ oxidation state in this sample. This is also supported by the energy position of the different features of the absorption edge, as better evidenced by the derivative curves shown in the lower panel of Figure 2. However, a significant broadening is present, suggesting the presence of a high degree of structural disorder in this sample.

Additional information can be obtained from the analysis of the pre-edge region ($E$ = 7116 eV), which shows a different structure for the S1 sample if compared to both to Fe$_3$O$_4$ and $\gamma$-Fe$_2$O$_3$ (Figure S2). The pre-edge peak originates from the dipole-forbidden 1s → 3d transition, and its intensity is determined by deviations from the centrosymmetric local structure of the Fe site and by the number of holes in the 3d states. The higher intensity found for CS1 compared to $\gamma$-Fe$_2$O$_3$ is therefore indicative of larger structural disorder and is compatible with the nanostructure, where a significant fraction of the $Fe^{3+}$ ions occupies surface/interface sites, possibly lacking the inversion symmetry.[50] To obtain more quantitative information, the pre-edge was analyzed by simulating the rising edge with a polynomial and then fitted using the minimum amount of Gaussian functions (Figure S2), corresponding to transitions toward the final 3d states (see Section 2 in the Supporting Information for a detailed description). For CS1, the energy separation between the final states $1s^1t_{2g}^4e_g^2$ and $1s^1t_{2g}^3e_g^3$ of $Fe^{3+}$ in the high-spin configuration in an octahedral crystal field was found to be lower than that


https://dx.doi.org/10.1021/acsanm.0c02588
ACS Appl. Nano Mater. 2021, 4, 1057–1066

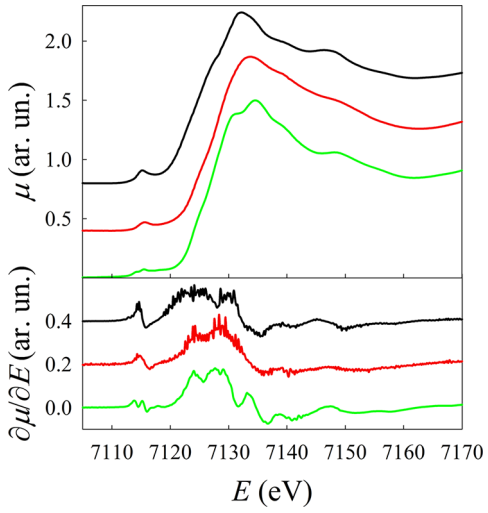


**Figure 2.** Fe K-edge XANES spectra of $Fe_3O_4$ (black line), $\gamma$-$Fe_2O_3$ (green line), and CS1 (red line). In the lower panel, the corresponding derivatives are shown. Spectra and derivatives have been shifted along the $y$ axis for the sake of clarity.

observed for maghemite, and the widths of all the three components are much larger than those of both reference samples. Both these pieces of evidence point toward a fairly distorted $Fe^{3+}$ local chemical environment, possibly encompassing also different geometries and different coordination numbers.

The magnetic behavior of Au@$FeO_x$ NPs was investigated by recording low-temperature (3 K) magnetization curves as a function of the applied magnetic field (Figure S4). For both core@shell samples, at low temperatures, a weak magnetic contribution with the s-like shape typical of superparamagnetic behavior was found overlapped to a much more intense diamagnetic component related to the gold domain, and it is completely negligible at room temperature. EPR spectra recorded at different temperatures (Figure S3) show only a weak signal. Their temperature dependence, where the line width increases with decreasing temperature, and the absence of signals attributable to isolated $Fe^{3+}$ exclude a simple paramagnetic behavior. The line broadening with lowering temperature suggests a progressive blocking of the magnetization direction on the time scale of the EPR experiment. In this respect, the results are in agreement with the presence of antiferromagnetic interactions in the iron oxide shell. These interactions leave as magnetic contribution at low temperature only that of the disordered layer of surface spins, whereas a superparamagnetic behavior is obtained at room temperature (see the Supporting Information for a more detailed discussion).

Although assigning a precise magnetic phase to the $FeO_x$ shell was not possible, all the performed characterizations suggest a disordered crystal and spin structure, where Fe ions have a +3 oxidation number and the superparamagnetic properties arising from surface spins are extremely weak at room temperature within the range of magnetic fields investigated. As a consequence, the iron oxide shell can be in fact treated as an ultrathin dielectric shell with a negligible magnetic response at room temperature.

**Optical and Magneto-optical Characterization.** In Figure 3a, the extinction spectra of the Au@$FeO_x$ NPs are shown, compared to the Au NPs used as seeds for the growth of the $FeO_x$ shell. The contributions from LSPR and interband transitions of Au (at higher energy) were deconvolved through a fitting with the sum of a Lorentzian and a Gaussian function, respectively, for the two components (Figure S5). The LSPR component is located at 2.38 eV (521 nm) for Au NPs dispersed in hexane solvent ($n$ = 1.37), as expected from Mie theory and in agreement with the literature on spherical gold

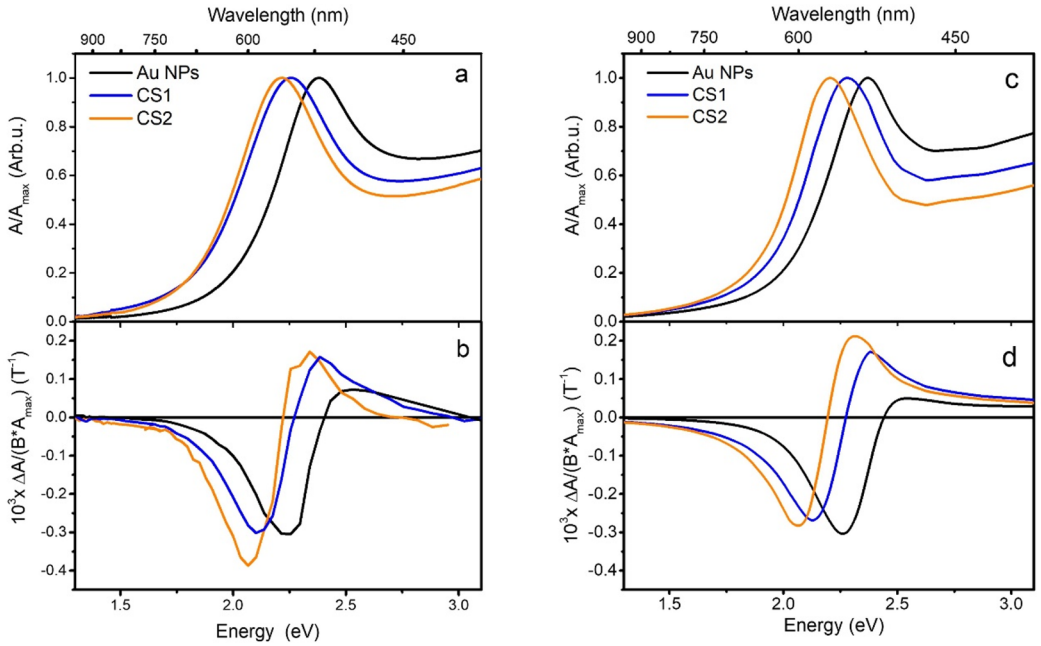


**Figure 3.** (a) Extinction spectra of Au NPs (black) and Au@$FeO_x$ NPs with 0.5 nm (CS1, blue) and 1 nm (CS2, orange) iron oxide shell thickness. All the curves are normalized to the maximum of the LSPR peak. (b) MCD spectra of the corresponding samples; (c, d) calculations of extinction and MCD spectra using the quasi-static core@shell polarizability. For CS1 and CS2, the experimental bulk dielectric function of maghemite is used for the shell. Both extinction and MCD are normalized for the extinction maximum. MCD is further normalized to the applied magnetic field.


https://dx.doi.org/10.1021/acsanm.0c02588
ACS Appl. Nano Mater. 2021, 4, 1057−1066

NPs with a similar mean size.[11,51,52] In Au@$FeO_x$ NPs, the LSPR peak is still present and experiences only a slight broadening, indicating that the formation of the iron oxide shell has a negligible damping action on Au NPs. On the other hand, the position of the plasmon resonance was found to be considerably modified by the presence of the iron oxide shell: in the NPs with shell thicknesses of 0.5 and 1.0 nm, the plasmonic peaks red-shift to 2.26 eV (549 nm) and 2.22 eV (559 nm), respectively. The red-shift of the plasmon resonance is a typical feature observed in Au−$FeO_x$ heterostructure nanocrystals,[53−56] and it can be explained within the framework of quasi-static Mie theory,[57,58] with the increase of the local refractive index around the Au NPs.[59]

In order to investigate how the $FeO_x$ shell affects the magnetic modulation of the LSPR of the Au core in our samples, room-temperature MCD spectroscopy was performed in the Faraday configuration. In Figure 3b, the MCD signal of Au and Au@$FeO_x$ NPs is normalized for the extinction maximum in order to take into account the different concentrations of the NP dispersions analyzed and for the applied magnetic field (1.35 T). The MCD spectrum of Au NPs shows a derivative line shape crossing zero at the energy of the LSPR extinction maximum. Such behavior is ascribed to the excitation of circular plasmonic modes involving conduction electrons of Au, driven by the incoming circularly polarized light (CP).[11,18,60] Such circular plasmonic modes can be considered as a two-fold degenerate state for plasmon excitation:[61] the application of a static magnetic field in the propagation direction of light perturbs the resonant conditions removing the degeneracy, and an MCD spectroscopic signal results from the differential absorption of two oppositely shifted circular plasmonic modes, excited by CP light with opposite helicity. The energy shift $\Delta E$ between the two circular plasmonic modes depends linearly on the magnetic field intensity. This is analogous to a simple two-level system with a degenerate excited state, responsible for the origin of the *A* term in the MCD quantum description,[62] commonly called a "diamagnetic" line shape, with the only difference being that in the case of LSPR, a collective excitation of all the free electron clouds of the metal NP occurs.

A similar line shape was observed also for Au@$FeO_x$ NPs, again crossing zero in correspondence with the respective LSPR extinction peak. In the MCD spectrum of an ideal non-interacting core@shell system, we would expect a sum of the MCD contribution of the two components, the Au core and a disordered maghemite shell. The MO contribution of pure maghemite is generally displayed in the MCD spectrum with a characteristic spectral fingerprint due to transitions between Zeeman-split electronic levels of the material, related to $Fe^{3+}$ ions, and its magnitude is proportional to the magnetization, which for pure maghemite NPs has a characteristic super-paramagnetic field dependence. However, no characteristic feature revealing the iron oxide contribution to the total MCD line shape was observed, consistent with the very low magnetic moment in the sample. This is also confirmed by the linear field dependence of the MCD signal for the core@shell NPs dispersed in a polymer matrix (Figure S6). The latter can be highlighted by comparison with the MO spectra of pure maghemite NPs of 5 nm size and similar concentration (Figure S7),[40] which clearly shows a different MO spectral fingerprint (with a broad positive peak at 2.7−3.0 eV) with respect to what is displayed by our samples. This behavior is even more remarkable if we consider that the MO response of iron oxide NP dispersions is usually 2−3 orders of magnitude greater than Au NP dispersion with similar concentration. Indeed, the latter is usually the dominant magneto-optical contribution in heterostructure Au−$FeO_x$ dimeric and flower-like NPs where the iron oxide domain is at least comparable in size to the Au core, completely masking the MO signature of the LSPR.[41] In our samples, since the volume fractions of the $FeO_x$ domain are 30 and 50% (10 and 20% in weight) for CS1 and CS2, respectively, such a volume of magnetite or maghemite would be expected to give a sizeable signal in MCD. These considerations, consistent with the magnetic and structural characterization performed, allow us to reasonably ascribe the MCD signal exclusively to the LSPR of Au.

Remarkably, despite the absence of any MO response for the iron oxide phase, the peak-to-peak intensity of the signal is increased by 18% for CS1 and 48% for CS2 with respect to uncoated Au NPs. This is even more surprising if we consider that the Fe oxide phase gives no contribution to the magnetization of the sample, ruling out the possibility of increasing the LSPR modulation through an increase in the local magnetic field at the Au/Fe oxide interface. The origin of such a significant enhancement of the MCD signal should thus be different.

Even though the peak-to-peak amplitude gives a reasonable indication of the magnetic field driven modulation of LSPR, it is also affected by other parameters, such as peak width. In order to get a more precise assessment of the magnetic modulation and to evaluate the effect of the iron oxide shell on the magneto-optical properties of the Au core, a detailed analysis of the spectra was performed, supported by analytical calculations of the extinction and MCD spectra.

The MCD of pure Au NPs was calculated analytically using the field- and helicity-dependent quasi-static polarizability (eq S1) and the related extinction cross section (eq S2) within the framework of an analytical model developed in previous work (see the Supporting Information for more details).[11,63]

A possible parameter that should be considered to explain the enhancement of the MO response in our core@shell nanostructures is the increase in value of the local dielectric function around the plasmonic core induced by the shell ($\varepsilon_s$). Indeed, in the spectral range investigated, iron oxide phases have a larger real part of the dielectric function with respect to the hexane solvent used to disperse the NPs.[64−66] It is the larger $\varepsilon_s$ of the shell that causes the red-shift in the extinction peak as well as an increase in the extinction cross section due to a higher quality factor of the resonance. Indeed, for Au NPs, a significant damping occurs when the LSPR is overlapped with interband transitions of Au (close to 500 nm), and the red-shift of the LSPR position reduces the overlapping, resulting in a sharper and more intense extinction cross section. In the MCD spectrum, the effect of the overlapping between LSPR and interband transitions is observed with the asymmetry of the signal, where the high energy lobe of the signal is the one which is closer to the interband transitions, and it is thus more damped.[11,67]

For samples CS1 and CS2, in order to consider the effect of the shell on the optical and MCD response, a core@shell model was employed for the quasi-static polarizability, according to Bohren and Huffman,[57] modified to take into account the magnetic field effect according to Gu and Kornev (Supporting Information).[63] Assuming that the magnetic field effect on the shell is small and comparable to that of the medium, as suggested by the low magnetic moment detected at


https://dx.doi.org/10.1021/acsanm.0c02588
ACS Appl. Nano Mater. 2021, 4, 1057−1066

**Table 1. Parameters and Results of the Fit of MCD Spectra[a]**

| | fixed parameters | | | free parameters | |
|---|---|---|---|---|---|
| sample | $I$ | $E_0$ (eV) | $\gamma$ (eV) | $\lvert\Delta E/B\rvert$ (eV/T) | $\delta I$ |
| Au NPs | 0.102 | 2.36 | 0.41 | $3.7 \times 10^{-5}$ (0.1) | $-9.8 \times 10^{-6}$ (0.5) |
| CS1 | 0.129 | 2.24 | 0.48 | $4.2 \times 10^{-5}$ (0.1) | $-6.0 \times 10^{-6}$ (0.1) |
| CS2 | 0.056 | 2.20 | 0.44 | $4.6 \times 10^{-5}$ (0.2) | $-5.6 \times 10^{-6}$ (0.5) |

[a] $I$, $\gamma$, and $E_0$: peak amplitude, width, and energy position of the plasmonic peak in extinction spectra, obtained by a fitting with a Lorentzian function; $\Delta E$: magnetic field-induced energy shift between circular magnetoplasmonic modes excited with RCP and LCP light, normalized for the applied field; $\delta I$: parameter that takes into account the asymmetry in the MCD line shape related to the presence of interband transitions.

room temperature, we can write a simplified equation for the quasi-static field- and helicity-dependent core@shell polarizability (eq 1).

$$\alpha(E,B) = \frac{4}{3}\pi(R+d)^3 \frac{(\varepsilon_s(E)-\varepsilon_m)(\varepsilon(E)+2\varepsilon_s(E)+B(f(E)-f_s)) + \left(\frac{R}{R+d}\right)^3(\varepsilon(E)-\varepsilon_s(E)+B(f(E)-f_s))(\varepsilon_m+2\varepsilon_s(E))}{(\varepsilon_s(E)+2\varepsilon_m)(\varepsilon(E)+2\varepsilon_s(E)+B(f(E)-f_s)) + \left(\frac{R}{R+d}\right)^3(\varepsilon(E)-\varepsilon_s(E)+B(f(E)-f_s))(2\varepsilon_s(E)-2\varepsilon_m)} \quad (1)$$

where $R$ and $d$ are the radius of the core and the shell thickness, respectively, $\varepsilon(E)$ and $\varepsilon_s(E)$ are the complex dielectric functions of the core and the shell, respectively, $\varepsilon_m$ is the dielectric constant of the solvent (hexane in our case), and $f(E)$ and $f_s$ are the coupling functions of the metal and the shell, respectively, describing the effect of the magnetic field (more details can be found in the Supporting Information). The extinction cross section and the MCD spectrum were calculated in analogy to the case of a pure metal sphere but using the core@shell polarizability. The bulk experimental dielectric function of Au is used for the core (from Johnson and Christy[68]) with size correction according to Kreibig and Vollmer.[58] Based on the XAS characterization performed, the dielectric function of bulk maghemite (taken from experimental data[66]) was chosen for the shell ($\varepsilon_s$), even if the disordered chemical structure detected is expected to induce changes in the dielectric function with respect to the bulk one. The calculation of extinction and MCD are reported in Figure 3c,d. The LSPR extinction peak position is reproduced correctly by the calculations, while the LSPR line width is larger in the experiments, probably due to a distribution in the shell thickness. In the calculated MCD spectra (Figure 3d), the increase of the peak-to-peak signal in the core@shell is consistent with that observed in the experiments, confirming the crucial role of the dielectric function of the shell in the enhancement of MCD. The differences between the experiment and the calculation are rather small and can be ascribed to small contributions of the MO transitions of the Fe oxide, which in first approximation are neglected in our analysis, to deviations of the permittivity of the shell with respect to bulk maghemite according to its disordered structure and to the effect of the magnetic field on the interband transition of Au, which are not considered in this treatment.

To further confirm that the increase of the peak-to-peak MCD signal of a Au nanosphere may arise form a dielectric effect, we also performed a calculation of the extinction and MCD spectra using the simple spherical model for the polarizability (eq S1) by tuning arbitrarily the medium permittivity ($\varepsilon_m$) to fit the experimental spectra (Figure S9). The experimental MCD is reproduced with excellent agreement by employing constant $\varepsilon_m$ values of 3.06 and 3.61, which are substantially larger than that of the solvent employed (1.89). This analysis strongly suggests that shifting the LSPR position toward the red region by changing the permittivity around the Au core is an effective strategy to enhance the MCD signal of Au NPs.

However, it would be interesting to unveil if it is a purely optical effect, which is transferred to the MCD spectrum, or if the magnetic modulation of LSPR is also affected from such changes in the permittivity of the surroundings.

As the magnitude of the peak-to-peak MCD signal is not exclusively affected by the magnetic modulation, a determination of the magnetic field-induced energy shift is necessary in order to estimate the magnetic modulation of LSPR in these nanostructures. To this aim, a fitting of the experimental MCD spectrum was performed, using a difference of two Lorentzian functions having the same parameters of the LSPR extinction peak (width and amplitude), each one shifted in the energy position by a quantity $\Delta E$, which represents the magnitude of the magnetic modulation of LSPR that originates from the MCD signal:

$$MCD(E) = \frac{2(I+\delta I)}{\pi} \bullet \frac{\gamma}{4(E-(E_0-\Delta E))^2+\gamma^2} - \frac{2(I-\delta I)}{\pi} \bullet \frac{\gamma}{4(E-(E_0+\Delta E))^2+\gamma^2} \quad (2)$$

where $I$ is the peak amplitude, $\gamma$ is the peak width, $E$ is the photon energy, and $E_0$ is the LSPR peak energy in eV. $\delta I$ is a phenomenological parameter introduced to reproduce the asymmetry in the MCD line shape related to the presence of interband transitions. Indeed, when the resonance moves far from the interband transitions, the extinction cross section increases: as a consequence, depending on RCP or LCP illumination, a slightly higher or lower intensity of the extinction occurs, resulting in asymmetric positive−negative lobes in the MCD spectrum. The fit is performed by keeping the values of $I$, $\gamma$, and $E_0$ fixed to those obtained in the fitting of the extinction spectra for the LSPR component (Figure S5, Table 1). Excellent agreement with the experimental data is displayed for the three samples investigated (Figure S8). The values of $\Delta E$ (Table 1) determined by this procedure were found to increase with thicker shells. Indeed, the energy shift


https://dx.doi.org/10.1021/acsanm.0c02588
ACS Appl. Nano Mater. 2021, 4, 1057−1066

increased with respect to uncoated Au NPs by a factor of 13 and 23% for CS1 and CS2, respectively. Furthermore, symmetry of the MCD line shape is gradually recovered in the presence of the shell due to the smaller overlapping with the interband transitions, as indicated by lower $\delta I$ values with increasing shell thickness.

According to the analytical model employed, an expression for the energy shift as a function of the LSPR energy ($E_0$) is obtained through the series expansion of the dielectric functions of the metal and the coupling function $f$. The coupling functions $f$ and $f_m$ describe the effect of the magnetic field on the metal, $f(E) = f_1(E) + if_2(E)$, and on the surrounding medium ($f_m$). According to the model, the energy shift induced by the magnetic field can be calculated through eq 3:[11]

$$\Delta E\ (E_0) = \frac{B\Delta f_1(E_0)}{\frac{\delta\varepsilon_1}{\delta E}\Big|_{E_0} + B\frac{\delta\Delta f_1(E)}{\delta E}\Big|_{E_0}} \approx \frac{B\Delta f_1(E_0)}{\frac{\delta\varepsilon_1}{\delta E}\Big|_{E_0}} \quad (3)$$

where $B$ is the applied magnetic field, $\Delta f_1(E) = f_1(E) - f_m$, $E_0$ represents the energy of the LSPR maximum, and the second term in the denominator can be neglected as it is smaller with respect to the first term. The dielectric functions are written here as a function of the photon energy $E$, and the derivatives of the real dielectric function ($\varepsilon_1$) are calculated at the energy of the LSPR extinction maximum ($E_0$). Using a Drude-like dielectric function, eq 3 can be approximated to a frequency-independent value, equal to half the cyclotron energy ($\Delta E = \frac{\hbar\omega_c}{2} = \hbar eB/2m^*$, where $e$ and $m^*$ are the electron charge and effective mass, respectively).[11,63] Nevertheless, it is well-known that for gold, the dielectric function is not rigorously Drude-like because of the presence of strong interband transitions in the visible range. As a consequence, the values of energy shift are more strongly affected by the position of the LSPR ($E_0$), i.e., by the values taken by $\varepsilon$ at that specific photon energy. This is confirmed by Figure 4, where an increase of the calculated $\Delta E$ with the red-shift of $E_0$ is clearly visible, reaching values close to $\hbar\omega_c/2$ only at low energies. The experimentally determined values of the energy shift for the three samples are plotted at their resonant energy $E_0$, together with the calculated curve, displaying reasonable agreement. The increase in the magnetoplasmonic performance due to the iron oxide shell can thus be ascribed to a purely optical effect, pointing out the crucial role of the dielectric function of the shell. Remarkably, the latter has also a positive effect on the magnetic modulation of LSPR. These findings can open the way for the enhancement of the MCD signal of Au by tuning the shell dielectric function and thickness. This can be exploited to increase the sensitivity of plasmonic sensing approaches based on magnetic modulation. Indeed, a larger modulation induces a steeper slope (increased by a factor 2 with respect to Au NPs) of the magneto-optical signal at the resonance condition, which in turn allows probing smaller variations in the local refractive index by monitoring changes in the intensity of the MCD signal at a fixed wavelength.[11]

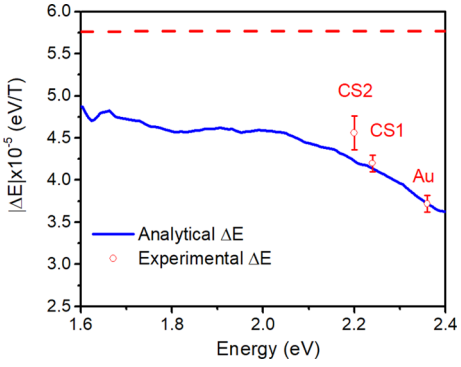


**Figure 4.** Calculated energy shift (blue line) compared to that experimentally determined with the fit of the MCD curve (red dots), plotted as a function of the LSPR energy. The vertical bars represent the standard deviation of the fit. The dashed red straight line represents $\hbar\omega_C/2$, which is the energy shift obtained using Drude dielectric functions.

According to Figure 4, a further increase of ~12% in the magnetic modulation can be obtained in Au nanospheres by shifting the LSPR to 2 eV, which can be achieved by embedding the nanoparticles in a $TiO_2$ matrix, which has a dielectric constant of 6.8 and low losses in the visible range.

## CONCLUSIONS

In summary, we prepared two different Au@$FeO_x$ core@shell NP samples with shell thicknesses of 0.5 and 1 nm starting from preformed Au NP seeds. The structural and magnetic characterization ruled out the emergence of sizeable magnetic and magneto-optical properties of the iron oxide shell. Despite this, the shells were found to induce a significant, thickness-dependent enhancement of the MCD signal of the plasmonic Au core. We developed an advanced fitting method to extract the magnetoplasmonic modulation amplitude from optical and magneto-optical spectra of plasmonic nanoparticles and compared these values with a finely tuned analytical model. Taken together, experiments and calculations strongly suggest that the increased magnetoplasmonic modulation induced by the ultrathin iron oxide shells is ultimately non-magnetic in nature but is in fact a dielectric effect. By shifting the LSPR at lower energies, far from the interband transitions of Au, the field splitting of magnetoplasmonic modes approaches the ideal value of $\hbar\omega_c/2$, valid for purely Drude-like metals. Our findings show a new approach to enhancing the magnetic modulation of LSPR without the need to add a large amount of magnetic phases, with the advantage of reducing the associated LSPR damping. Finally, we conclude that the intensity of the magnetoplasmonic response critically depends on the values of the complex dielectric function of the (magneto)plasmonic material at the resonance frequency. By applying the proposed model, a quantitative prediction of the magnitude of the magnetoplasmonic effect can be obtained given the dielectric function of the shell material. This represents an extremely powerful predictive tool for the rational design of magneto-plasmonic architectures with optimized performance. Such optimized dielectric-coated plasmonic nanostructures can be used as a magnetoplasmonic substrate with improved sensitivity for direct and indirect plasmonic sensing exploiting magnetic modulation of LSPR. The strategy proposed can be applied to different nanostructures or combined to other approaches to improve the MO signal, e.g., the use of periodic structures supporting surface lattice resonance.[69,70] In addition, other promising applications of magnetophotonic nanostructures,[71] such as plasmon rulers,[72] optical isolation,[15] or opto-magnetism,[17] can be potentially improved through our proposed strategy. Looking beyond magnetic modulation of


https://dx.doi.org/10.1021/acsanm.0c02588
ACS Appl. Nano Mater. 2021, 4, 1057−1066

the plasmonic response, the Au@$FeO_x$ nanostructures presented in this work broaden the library of bifunctional Au−iron oxide heterostructures[73] that can be used in catalysis and photocatalysis,[74−77] coupling the optically active core with a thin shell that acts as a functional catalyst while maintaining the plasmonic properties of the core.

## ■ ASSOCIATED CONTENT

### Supporting Information

The Supporting Information is available free of charge at https://pubs.acs.org/doi/10.1021/acsanm.0c02588.

Size distribution of the nanoparticle samples; additional details on the analysis of pre-edge peak of XAS spectra; EPR spectra; *M vs H* curves recorded at 3 K; field dependence of the MCD signal at fixed wavelength for sample CS2; magnetic circular dichroism spectrum of maghemite nanoparticles; fit of the extinction and MCD spectra; details on the calculation of the extinction and MCD spectra (PDF)

## ■ AUTHOR INFORMATION


### Corresponding Author

**Francesco Pineider** − *INSTM and Department of Chemistry and Industrial Chemistry, Università di Pisa, 56124 Pisa, Italy;* orcid.org/0000-0003-4066-4031; Email: francesco.pineider@unipi.it

### Authors

**Alessio Gabbani** − *INSTM and Department of Chemistry and Industrial Chemistry, Università di Pisa, 56124 Pisa, Italy;* orcid.org/0000-0002-4078-0254

**Elvira Fantechi** − *INSTM and Department of Chemistry and Industrial Chemistry, Università di Pisa, 56124 Pisa, Italy;* orcid.org/0000-0002-9323-2198

**Gaia Petrucci** − *INSTM and Department of Chemistry and Industrial Chemistry, Università di Pisa, 56124 Pisa, Italy;* orcid.org/0000-0001-8071-4561

**Giulio Campo** − *INSTM and Department of Chemistry "U. Schiff", Università degli Studi di Firenze, 50019 Sesto Fiorentino, Italy;* orcid.org/0000-0003-3777-4520

**César de Julián Fernández** − *CNR-IMEM, 43124 Parma, Italy;* orcid.org/0000-0002-6671-2743

**Paolo Ghigna** − *Department of Chemistry, Università di Pavia, 27100 Pavia, Italy;* orcid.org/0000-0002-8680-7272

**Lorenzo Sorace** − *INSTM and Department of Chemistry "U. Schiff", Università degli Studi di Firenze, 50019 Sesto Fiorentino, Italy;* orcid.org/0000-0003-4785-1331

**Valentina Bonanni** − *INSTM and Department of Chemistry "U. Schiff", Università degli Studi di Firenze, 50019 Sesto Fiorentino, Italy;* orcid.org/0000-0001-8346-0069

**Massimo Gurioli** − *Department of Physics and Astronomy, Università degli Studi di Firenze, 50019 Sesto Fiorentino, FI, Italy;* orcid.org/0000-0002-6779-1041

**Claudio Sangregorio** − *CNR-ICCOM, 50019 Sesto Fiorentino, FI, Italy; INSTM and Department of Chemistry "U. Schiff", Università degli Studi di Firenze, 50019 Sesto Fiorentino, Italy;* orcid.org/0000-0002-2655-3901

Complete contact information is available at: https://pubs.acs.org/10.1021/acsanm.0c02588

### Author Contributions

[▽]A.G. and E.F. contributed equally to this work.


### Notes

The authors declare no competing financial interest.

## ■ ACKNOWLEDGMENTS

Authors acknowledge the financial support of H2020-FETOPEN-2016-2017 Grant No. 737709 FEMTOTERABYTE (EC) and of PRA_2017_25 (Università di Pisa). E.F. acknowledges fellowship Galileo Galilei (Università di Pisa).

## ■ REFERENCES


(1) Anker, J. N.; Hall, W. P.; Lyandres, O.; Shah, N. C.; Zhao, J.; Van Duyne, R. P. Biosensing with Plasmonic Nanosensors. *Nat. Mater.* **2008**, *7*, 442−453.

(2) Mayer, K. M.; Hafner, J. H. Localized Surface Plasmon Resonance Sensors. *Chem. Rev.* **2011**, *111*, 3828−3857.

(3) Larsson, E. M.; Syrenova, S.; Langhammer, C. Nanoplasmonic Sensing for Nanomaterials Science. *Nanophotonics* **2012**, *1*, 249−266.

(4) Lal, S.; Link, S.; Halas, N. J. Nano-Optics from Sensing to Waveguiding. *Nat. Photonics* **2007**, *1*, 641−648.

(5) Krasavin, A. V.; Zheludev, N. I. Active Plasmonics: Controlling Signals in Au/Ga Waveguide Using Nanoscale Structural Transformations. *Appl. Phys. Lett.* **2004**, *84*, 1416−1418.

(6) MacDonald, K. F.; Sámson, Z. L.; Stockman, M. I.; Zheludev, N. I. Ultrafast Active Plasmonics. *Nat. Photonics* **2009**, *3*, 55−58.

(7) Pacifici, D.; Lezec, H. J.; Atwater, H. A. All-Optical Modulation by Plasmonic Excitation of CdSe Quantum Dots. *Nat. Photonics* **2007**, *1*, 402−406.

(8) Wei, H.; Pan, D.; Zhang, S.; Li, Z.; Li, Q.; Liu, N.; Wang, W.; Xu, H. Plasmon Waveguiding in Nanowires. *Chem. Rev.* **2018**, *118*, 2882−2926.

(9) Böhme, A.; Sterl, F.; Kath, E.; Ubl, M.; Manninen, V.; Giessen, H. Electrochemistry on Inverse Copper Nanoantennas: Active Plasmonic Devices with Extraordinarily Large Resonance Shift. *ACS Photonics* **2019**, *6*, 1863−1868.

(10) Nguyen, M.; Sun, X.; Lacaze, E.; Winkler, P. M.; Hohenau, A.; Krenn, J. R.; Bourdillon, C.; Lamouri, A.; Grand, J.; Lévi, G.; Boubekeur-Lecaque, L.; Mangeney, C.; Félidj, N. Engineering Thermoswitchable Lithographic Hybrid Gold Nanorods as Plasmonic Devices for Sensing and Active Plasmonics Applications. *ACS Photonics* **2015**, *2*, 1199−1208.

(11) Pineider, F.; Campo, G.; Bonanni, V.; de Julián Fernández, C.; Mattei, G.; Caneschi, A.; Gatteschi, D.; Sangregorio, C. Circular Magnetoplasmonic Modes in Gold Nanoparticles. *Nano Lett.* **2013**, *13*, 4785−4789.

(12) Maccaferri, N.; Gregorczyk, K. E.; de Oliveira, T. V. A. G.; Kataja, M.; van Dijken, S.; Pirzadeh, Z.; Dmitriev, A.; Åkerman, J.; Knez, M.; Vavassori, P. Ultrasensitive and Label-Free Molecular-Level Detection Enabled by Light Phase Control in Magnetoplasmonic Nanoantennas. *Nat. Commun.* **2015**, *6*, 6150.

(13) Temnov, V. V.; Armelles, G.; Woggon, U.; Guzatov, D.; Cebollada, A.; Garcia-Martin, A.; Garcia-Martin, J.-M.; Thomay, T.; Leitenstorfer, A.; Bratschitsch, R. Active Magneto-Plasmonics in Hybrid Metal−Ferromagnet Structures. *Nat. Photonics* **2010**, *4*, 107−111.

(14) Armelles, G.; Cebollada, A.; García-Martín, A.; González, M. U. Magnetoplasmonics: Magnetoplasmonics: Combining Magnetic and Plasmonic Functionalities. *Adv. Opt. Mater.* **2013**, *1*, 2−2.

(15) Floess, D.; Giessen, H. Nonreciprocal Hybrid Magnetoplasmonics. *Rep. Prog. Phys.* **2018**, *81*, 116401.

(16) Bossini, D.; Belotelov, V. I.; Zvezdin, A. K.; Kalish, A. N.; Kimel, A. V. Magnetoplasmonics and Femtosecond Optomagnetism at the Nanoscale. *ACS Photonics* **2016**, *3*, 1385−1400.

(17) Cheng, O. H.-C.; Son, D. H.; Sheldon, M. Light-Induced Magnetism in Plasmonic Gold Nanoparticles. *Nat. Photonics* **2020**, *14*, 365−368.

(18) Sepúlveda, B.; González-Díaz, J. B.; García-Martín, A.; Lechuga, L. M.; Armelles, G. Plasmon-Induced Magneto-Optical Activity in Nanosized Gold Disks. *Phys. Rev. Lett.* **2010**, *104*, 147401.
(19) Manera, M. G.; Colombelli, A.; Taurino, A.; Martin, A. G.; Rella, R. Magneto-Optical Properties of Noble-Metal Nanostructures: Functional Nanomaterials for Bio Sensing. *Sci. Rep.* **2018**, *8*, 12640.
(20) González-Díaz, J. B.; García-Martín, A.; Armelles, G.; Navas, D.; Vázquez, M.; Nielsch, K.; Wehrspohn, R. B.; Gösele, U. Enhanced Magneto-Optics and Size Effects in Ferromagnetic Nanowire Arrays. *Adv. Mater.* **2007**, *19*, 2643−2647.
(21) Bonanni, V.; Bonetti, S.; Pakizeh, T.; Pirzadeh, Z.; Chen, J.; Nogués, J.; Vavassori, P.; Hillenbrand, R.; Åkerman, J.; Dmitriev, A. Designer Magnetoplasmonics with Nickel Nanoferromagnets. *Nano Lett.* **2011**, *11*, 5333−5338.
(22) Maccaferri, N.; Berger, A.; Bonetti, S.; Bonanni, V.; Kataja, M.; Qin, Q. H.; Van Dijken, S.; Pirzadeh, Z.; Dmitriev, A.; Nogués, J.; Åkerman, J.; Vavassori, P. Tuning the Magneto-Optical Response of Nanosize Ferromagnetic Ni Disks Using the Phase of Localized Plasmons. *Phys. Rev. Lett.* **2013**, *111*, 167401.
(23) Armelles, G.; Caballero, B.; Cebollada, A.; Garcia-Martin, A.; Meneses-Rodríguez, D. Magnetic Field Modification of Optical Magnetic Dipoles. *Nano Lett.* **2015**, *15*, 2045−2049.
(24) González-Díaz, J. B.; García-Martín, A.; García-Martín, J. M.; Cebollada, A.; Armelles, G.; Sepúlveda, B.; Alaverdyan, Y.; Käll, M. Plasmonic Au/Co/Au Nanosandwiches with Enhanced Magneto-Optical Activity. *Small* **2008**, *4*, 202−205.
(25) Du, G. X.; Mori, T.; Saito, S.; Takahashi, M. Shape-Enhanced Magneto-Optical Activity: Degree of Freedom for Active Plasmonics. *Phys. Rev. B: Condens. Matter Mater. Phys.* **2010**, *82*, 161403.
(26) Du, G. X.; Mori, T.; Suzuki, M.; Saito, S.; Fukuda, H.; Takahashi, M. Magneto-optical effects in nanosandwich array with plasmonic structure of Au/$[Co/Pt]_n$/Au. *J. Appl. Phys.* **2010**, *107*, 09A928−09A924.
(27) Du, G. X.; Mori, T.; Suzuki, M.; Saito, S.; Fukuda, H.; Takahashi, M. Evidence of Localized Surface Plasmon Enhanced Magneto-Optical Effect in Nanodisk Array. *Appl. Phys. Lett.* **2010**, *96*, 081915.
(28) López-Ortega, A.; Zapata-Herrera, M.; Maccaferri, N.; Pancaldi, M.; Garcia, M.; Chuvilin, A.; Vavassori, P. Enhanced Magnetic Modulation of Light Polarization Exploiting Hybridization with Multipolar Dark Plasmons in Magnetoplasmonic Nanocavities. *Light: Sci. Appl.* **2020**, *9*, 49.
(29) Pappas, S. D.; Lang, P.; Eul, T.; Hartelt, M.; García-Martín, A.; Hillebrands, B.; Aeschlimann, M.; Papaioannou, E. T. Near-Field Mechanism of the Enhanced Broadband Magneto-Optical Activity of Hybrid Au Loaded Bi:YIG. *Nanoscale* **2020**, *12*, 7309−7314.
(30) Gilroy, K. D.; Ruditskiy, A.; Peng, H.-C.; Qin, D.; Xia, Y. Bimetallic Nanocrystals: Syntheses, Properties, and Applications. *Chem. Rev.* **2016**, *116*, 10414−10472.
(31) Ha, M.; Kim, J.-H.; You, M.; Li, Q.; Fan, C.; Nam, J.-M. Multicomponent Plasmonic Nanoparticles: From Heterostructured Nanoparticles to Colloidal Composite Nanostructures. *Chem. Rev.* **2019**, 12208.
(32) Cathcart, N.; Murshid, N.; Campbell, P.; Kitaev, V. Selective Plasmonic Sensing and Highly Ordered Metallodielectrics via Encapsulation of Plasmonic Metal Nanoparticles with Metal Oxides. *ACS Appl. Nano Mater.* **2018**, *1*, 6514−6524.
(33) Smolensky, E. D.; Neary, M. C.; Zhou, Y.; Berquo, T. S.; Pierre, V. C. $Fe_3O_4$@organic@Au: core−shell nanocomposites with high saturation magnetisation as magnetoplasmonic MRI contrast agents. *Chem. Commun.* **2011**, *47*, 2149−2151.
(34) Levin, C. S.; Hofmann, C.; Ali, T. A.; Kelly, A. T.; Morosan, E.; Nordlander, P.; Whitmire, K. H.; Halas, N. J. Magnetic−Plasmonic Core−Shell Nanoparticles. *ACS Nano* **2009**, *3*, 1379−1388.
(35) Borri, C.; Albino, M.; Innocenti, C.; Pineider, F.; Cavigli, L.; Centi, S.; Sangregorio, C.; Ratto, F.; Pini, R. A Bionic Shuttle Carrying Multi-Modular Particles and Holding Tumor-Tropic Features. *Mater. Sci. Eng., C* **2020**, *117*, 111338.
(36) López-Ortega, A.; Takahashi, M.; Maenosono, S.; Vavassori, P. Plasmon Induced Magneto-Optical Enhancement in Metallic Ag/FeCo Core/Shell Nanoparticles Synthesized by Colloidal Chemistry. *Nanoscale* **2018**, 18672.
(37) Wang, L.; Clavero, C.; Huba, Z.; Carroll, K. J.; Carpenter, E. E.; Gu, D.; Lukaszew, R. A. Plasmonics and Enhanced Magneto-Optics in Core−Shell Co−Ag Nanoparticles. *Nano Lett.* **2011**, *11*, 1237−1240.
(38) Wang, L.; Yang, K.; Clavero, C.; Nelson, A. J.; Carroll, K. J.; Carpenter, E. E.; Lukaszew, R. A. Localized Surface Plasmon Resonance Enhanced Magneto-Optical Activity in Core-Shell Fe−Ag Nanoparticles. *J. Appl. Phys.* **2010**, *107*, No. 09B303.
(39) Li, Y.; Zhang, Q.; Nurmikko, A. V.; Sun, S. Enhanced Magnetooptical Response in Dumbbell-like Ag−$CoFe_2O_4$ Nanoparticle Pairs. *Nano Lett.* **2005**, *5*, 1689−1692.
(40) Campo, G.; Pineider, F.; Bonanni, V.; Albino, M.; Caneschi, A.; de Julián Fernández, C.; Innocenti, C.; Sangregorio, C. Magneto-Optical Probe for Investigation of Multiphase Fe Oxide Nanosystems. *Chem. Mater.* **2015**, *27*, 466−473.
(41) Fantechi, E.; Innocenti, C.; Bertoni, G.; Sangregorio, C.; Pineider, F. Modulation of the Magnetic Properties of Gold-Spinel Ferrite Heterostructured Nanocrystals. *Nano Res.* **2020**, *13*, 785−794.
(42) Larsson, E. M.; Langhammer, C.; Zorić, I.; Kasemo, B. Nanoplasmonic Probes of Catalytic Reactions. *Science* **2009**, *326*, 1091−1094.
(43) Langhammer, C.; Larsson, E. M.; Kasemo, B.; Zorić, I. Indirect Nanoplasmonic Sensing: Ultrasensitive Experimental Platform for Nanomaterials Science and Optical Nanocalorimetry. *Nano Lett.* **2010**, *10*, 3529−3538.
(44) Tokarev, I.; Tokareva, I.; Gopishetty, V.; Katz, E.; Minko, S. Specific Biochemical-to-Optical Signal Transduction by Responsive Thin Hydrogel Films Loaded with Noble Metal Nanoparticles. *Adv. Mater.* **2010**, *22*, 1412−1416.
(45) Lei, D. Y.; Appavoo, K.; Sonnefraud, Y.; Haglund, R. F., Jr.; Maier, S. A. Single-particle plasmon resonance spectroscopy of phase transition in vanadium dioxide. *Opt Lett.* **2010**, *35*, 3988−3990.
(46) Szwarcman, D.; Vestler, D.; Markovich, G. The Size-Dependent Ferroelectric Phase Transition in $BaTiO_3$ Nanocrystals Probed by Surface Plasmons. *ACS Nano* **2011**, *5*, 507−515.
(47) Yu, H.; Chen, M.; Rice, P. M.; Wang, S. X.; White, R. L.; Sun, S. Dumbbell-like Bifunctional Au−$Fe_3O_4$ Nanoparticles. *Nano Lett.* **2005**, *5*, 379−382.
(48) D'Acapito, F.; Colonna, S.; Pascarelli, S.; Antonioli, G.; Balerna, A.; Bazzini, A.; Boscherini, F.; Campolungo, F.; Chini, G.; Dalba, G.; Davoli, I.; Fornasini, P.; Graziola, R.; Licheri, G.; Meneghini, C.; Rocca, F.; Sangiorgio, L.; Sciarra, V.; Tullio, V.; Mobilio, S. GILDA (Italian Beamline) on BM29. *ESRF Newsletter* **1998**, *30*, 42−44.
(49) Mason, W. R. *A Practical Guide to Magnetic Circular Dichroism Spectroscopy*; Wiley-Interscience: Hoboken, N.J., 2007.
(50) Wilke, M.; Farges, F.; Petit, P.-E.; Brown, G. E., Jr.; Martin, F. Oxidation state and coordination of Fe in minerals: An Fe K-XANES spectroscopic study. *Am. Mineral.* **2001**, *86*, 714−730.
(51) Bastús, N. G.; Comenge, J.; Puntes, V. Kinetically Controlled Seeded Growth Synthesis of Citrate-Stabilized Gold Nanoparticles of up to 200 nm: Size Focusing versus Ostwald Ripening. *Langmuir* **2011**, *27*, 11098−11105.
(52) Hiramatsu, H.; Osterloh, F. E. A Simple Large-Scale Synthesis of Nearly Monodisperse Gold and Silver Nanoparticles with Adjustable Sizes and with Exchangeable Surfactants. *Chem. Mater.* **2004**, *16*, 2509−2511.
(53) Fantechi, E.; Roca, A. G.; Sepúlveda, B.; Torruella, P.; Estradé, S.; Peiró, F.; Coy, E.; Jurga, S.; Bastús, N. G.; Nogués, J.; Puntes, V. Seeded Growth Synthesis of Au−$Fe_3O_4$ Heterostructured Nanocrystals: Rational Design and Mechanistic Insights. *Chem. Mater.* **2017**, *29*, 4022−4035.
(54) Umut, E.; Pineider, F.; Arosio, P.; Sangregorio, C.; Corti, M.; Tabak, F.; Lascialfari, A.; Ghigna, P. Magnetic, Optical and Relaxometric Properties of Organically Coated Gold−Magnetite (Au−$Fe_3O_4$) Hybrid Nanoparticles for Potential Use in Biomedical Applications. *J. Magn. Magn. Mater.* **2012**, *324*, 2373−2379.


https://dx.doi.org/10.1021/acsanm.0c02588
*ACS Appl. Nano Mater.* 2021, 4, 1057−1066

(55) Wei, Y.; Klajn, R.; Pinchuk, A. O.; Grzybowski, B. A. Synthesis, Shape Control, and Optical Properties of Hybrid Au/$Fe_3O_4$ "Nanoflowers". *Small* **2008**, *4*, 1635−1639.
(56) Shi, W.; Zeng, H.; Sahoo, Y.; Ohulchanskyy, T. Y.; Ding, Y.; Wang, Z. L.; Swihart, M.; Prasad, P. N. A General Approach to Binary and Ternary Hybrid Nanocrystals. *Nano Lett.* **2006**, *6*, 875−881.
(57) *Absorption and Scattering of Light by Small Particles*; Bohren, C. F.; Huffman, D. R., Eds.; Wiley-VCH Verlag GmbH: Weinheim, Germany, 1998. DOI: 10.1002/9783527618156.
(58) Kreibig, U.; Vollmer, M. *Optical Properties of Metal Clusters*; Springer-Verlag: Berlin, 1995.
(59) Palik, E. D. *Handbook of Optical Constants of Solids*; Academic Press: Orlando, FL, 1985.
(60) Du, G.-X.; Saito, S.; Takahashi, M. Magnetic Field Effect on the Localized Plasmon Resonance in Patterned Noble Metal Nanostructures. *IEEE Trans. Magn.* **2011**, *47*, 3167−3169.
(61) Weick, G.; Weinmann, D. Lifetime of the Surface Magnetoplasmons in Metallic Nanoparticles. *Phys. Rev. B* **2011**, *83*, 125405.
(62) Piepho, S. B.; Schatz, P. N. *Group Theory in Spectroscopy with Applications to Magnetic Circular Dichroism*; Wiley-Interscience: New York, 1983.
(63) Gu, Y.; Kornev, K. G. Plasmon Enhanced Direct and Inverse Faraday Effects in Non-Magnetic Nanocomposites. *J. Opt. Soc. Am. B* **2010**, *27*, 2165−2173.
(64) Querry, M. R. *Optical Constants*; MISSOURI UNIV-KANSAS CITY: 1985.
(65) Fontijn, W. F. J.; van der Zaag, P. J.; Devillers, M. A. C.; Brabers, V. A. M.; Metselaar, R. Optical and magneto-optical polar Kerr spectra of $Fe_3O_4$ and $Mg^{2+}$- or $Al^{3+}$-substituted $Fe_3O_4$. *Phys. Rev. B* **1997**, *56*, 5432−5442.
(66) Battie, Y.; Stchakovsky, M.; Neveu, S.; Jamon, D.; Garcia-Caurel, E. Synthesis and Study of $\gamma$-$Fe_2O_3$ and $CoFe_2O_4$ Based Ferrofluids by Means of Spectroscopic Mueller Matrix Ellipsometry. *J. Vac. Sci. Technol., B: Microelectron. Process. Phenom.* **2019**, *37*, No. 062929.
(67) Kovalenko, O.; Vomir, M.; Donnio, B.; Gallani, J. L.; Rastei, M. V. Chiromagnetoptics of Au and Ag Nanoparticulate Systems. *J. Phys. Chem. C* **2020**, *124*, 21722−21729.
(68) Johnson, P. B.; Christy, R.-W. Optical Constants of the Noble Metals. *Phys. Rev. B* **1972**, *6*, 4370.
(69) Pourjamal, S.; Kataja, M.; Maccaferri, N.; Vavassori, P.; van Dijken, S. Hybrid Ni/$SiO_2$/Au Dimer Arrays for High-Resolution Refractive Index Sensing. *Nanophotonics* **2018**, *7*, 905−912.
(70) Kataja, M.; Pourjamal, S.; van Dijken, S. Magnetic Circular Dichroism of Non-Local Surface Lattice Resonances in Magnetic Nanoparticle Arrays. *Opt. Express* **2016**, *24*, 3562.
(71) Maccaferri, N.; Zubritskaya, I.; Razdolski, I.; Chioar, I.-A.; Belotelov, V.; Kapaklis, V.; Oppeneer, P. M.; Dmitriev, A. Nanoscale Magnetophotonics. *J. Appl. Phys.* **2020**, *127*, No. 080903.
(72) Zubritskaya, I.; Lodewijks, K.; Maccaferri, N.; Mekonnen, A.; Dumas, R. K.; Åkerman, J.; Vavassori, P.; Dmitriev, A. Active Magnetoplasmonic Ruler. *Nano Lett.* **2015**, *15*, 3204−3211.
(73) Canet-Ferrer, J.; Albella, P.; Ribera, A.; Usagre, J. V.; Maier, S. A. Hybrid Magnetite−Gold Nanoparticles as Bifunctional Magnetic−Plasmonic Systems: Three Representative Cases. *Nanoscale Horiz.* **2017**, *2*, 205−216.
(74) Strickler, A. L.; Escudero-Escribano, M.; Jaramillo, T. F. Core−Shell Au@Metal-Oxide Nanoparticle Electrocatalysts for Enhanced Oxygen Evolution. *Nano Lett.* **2017**, *17*, 6040−6046.
(75) Wang, C.; Yin, H.; Dai, S.; Sun, S. A General Approach to Noble Metal−Metal Oxide Dumbbell Nanoparticles and Their Catalytic Application for CO Oxidation. *Chem. Mater.* **2010**, *22*, 3277−3282.
(76) Gellé, A.; Jin, T.; de la Garza, L.; Price, G. D.; Besteiro, L. V.; Moores, A. Applications of Plasmon-Enhanced Nanocatalysis to Organic Transformations. *Chem. Rev.* **2020**, *120*, 986−1041.
(77) Mishra, P.; Patnaik, S.; Parida, K. An Overview of Recent Progress on Noble Metal Modified Magnetic $Fe_3O_4$ for Photocatalytic Pollutant Degradation and $H_2$ Evolution. *Catal. Sci. Technol.* **2019**, *9*, 916−941.


https://dx.doi.org/10.1021/acsanm.0c02588
*ACS Appl. Nano Mater.* 2021, 4, 1057−1066